Conceptual Design of a Novel Particle-Based Soft Grasping Gripper

Chen, Qianyi; Schott, Dingena; Jovanova, Jovana

DOI
10.1115/1.4062647

Publication date
2024

Document Version
Final published version

Published in
Journal of Mechanisms and Robotics

ASME Journal of Mechanisms and Robotics
Online journal at:
https://asmedigitalcollection.asme.org/mechanismsrobotics

Conceptual Design of a Novel Particle-Based Soft Grasping Gripper

Qianyi Chen[1]
Faculty of Mechanical, Maritime, and Materials Engineering,
Delft University of Technology,
Delft 2628 CD, The Netherlands
e-mail: q.chen-5@tudelft.nl

Dingena Schott
Faculty of Mechanical, Maritime, and Materials Engineering,
Delft University of Technology,
Delft 2628 CD, The Netherlands
e-mail: d.l.schott@tudelft.nl

Jovana Jovanova
Faculty of Mechanical, Maritime, and Materials Engineering,
Delft University of Technology,
Delft 2628 CD, The Netherlands
e-mail: j.jovanova@tudelft.nl

Soft grippers show adaptability and flexibility in grasping irregularly shaped and fragile objects. However, the low loading capacity and less deformation limit the soft gripper for developing large-scale applications. To overcome these limitations, we propose a new concept of a soft actuator with engineered smart particles. The proposed soft actuator is a dual-chamber programmable structure made from an elastic membrane filled with different particles, which can be driven by expanding particle volume or flexible membrane shrinking. Compared to traditional pneumatic or particle-jamming actuators, we use a combination of granular materials and smart materials, which delivers better active performances of large-scale deformation and variable stiffness. The coupled numerical model of the discrete element method and the finite element method is used to demonstrate the concept. The results indicated that the proposed soft gripper achieves the functionality of large deformation by a shrinking membrane or expanding particles. By controlling different design parameters, the actuator bends up to 138 deg, and the stiffness is up to a maximum of nine times of the pneumatic actuator. Additionally, the bending angle and deflections of the gripper actuator first increase and then drop down with increasing particle diameter ratio, actuator length, and elastic modulus of membrane material. Hence, the choice of different parameters must be in a specific range to achieve the required deformation. In conclusion, the soft-grasping gripper actuator can realize large bending deformation and shows potential for developing soft grippers in multi-scale physical scenarios.
[DOI: 10.1115/1.4062647]

Keywords: compliant mechanisms, soft robotics

1 Introduction

Grasping complex objects has always been a challenge in the field of robotics. Robot grippers, which contact objects directly, need to interact with the environment or human beings to perform various tasks in different application scenarios such as automated production processes [1], minimally invasive procedures [2], and space exploration [3]. Traditional robotic grippers always rely on low mechanical flexibility controllers which attach to complex sensors and predefined kinematics systems, which perform poorly when grasping irregular, soft, or fragile objects [4,5]. However, with the development of robotics research, the emergence of soft robotics has allowed robots to meet more requirements on complex tasks [6].

Soft robots are composed of compliant components and actuators, which can achieve highly flexible behaviors. Soft grippers, which play an essential role in the soft robotic field, have excellent mechanical properties and interaction capabilities because of the soft material body and highly adaptable actuators [7,8]. Hence, the soft grippers demonstrate safety, adaptability, and operability when meeting complex gripping tasks, especially in unpredictable environments [9].

Soft grippers can be powered by different kinds of actuators that use different methods: electrical or magnetic charge [10,11], shape-memory effect [12], chemical reaction [13], and fluidic pressures [14]. Electrical or magnetic charge actuators, which respond to electric or magnetic fields, exhibit more significant deformation in angular or linear motion. Based on the electrical actuator, electroactive polymer materials and dielectric elastomers have been applied in soft grippers, which can achieve expansion and contraction changes [15,16]. In addition, a bionic gripper with a combination of magnetically responsive materials and a non-contact magnetic field, which can achieve rapid response to control command, has also been manufactured [17]. Nevertheless, low rigidity, low driving force, and poor controllability restrict the application of electrical or magnetic charge actuators. Coincidentally, the shape-memory materials, as the type of active response material, provide new strategies for manufacturing the soft gripper. As typical shape-memory materials, shape-memory alloy (SMA) and shape-memory polymer (SMP) respond fast and have large deformations when being stimulated by external environment change [18,19]. SMA is usually made into springs to achieve grasping tasks that meet large strains and stresses. Similarly, as various physical fields can stimulate the smart material, SMP is generally used to

[1]Corresponding author.

Contributed by the Mechanisms and Robotics Committee of ASME for publication in the Journal of Mechanisms and Robotics. Manuscript received November 18, 2022; final manuscript received May 22, 2023; published online June 26, 2023. Assoc. Editor: Irene Fassi.

realize the precise active control of the soft gripper [20,21]. However, the unpredictability of the intermediate state and low stiffness are the main disadvantages of shape-memory materials. Therefore, only using shape-memory materials is hard to ensure an accurate grasping process and offer sufficient contact force using grippers made simply of SMA or SMP. Besides, the actuators based on chemical reactions, such as combustion and catalytic decomposition, also actively provide power [7,22]. However, there is less power generated using a chemical reaction actuator in a limited time, which leads to difficulty in achieving continuous grasping work. As the most studied driving method, fluidic pressure actuators have many applications. Pneu-Net actuator, the first fluidic pressure actuator, has achieved large deformations by using multiple air cavities [23]. Based on the Pneu-Net actuator, the soft gripper with responsiveness and large deformations is designed to realize multi-functional grasping tasks [24]. In terms of matching ways, fiber-reinforced threads [25], strain-limited layers [26], and uneven wall thicknesses [27] have also been applied to the pneumatic actuator driving gripper to precisely control the expansion range. However, trapped by structural strength, actuator accessories, and high-pressure source, the pneumatic performs poorly in heavy loads and complex scenarios.

Flexible grippers typically perform well under the support of various actuators. However, limited to the compliance and the lack of robustness of the soft materials, soft robotic grippers have always been used on objects across a range of scales only from hundreds of micrometers to a few centimeters and perform poorly with large scale or heavy objects [28]. Inspiringly, the promising properties of using the jamming effect in stiffness variation bring the possibility of solving this problem [29]. The particle-jamming effect, as versatile jamming, is widely used in soft robotic grippers [30]. The primary mechanism of particle jamming is the particle packing state's transition. Initially, the particles are first capsuled loosely and show the natural packing state, which allows particles to flow within the membrane. However, when the particle packing state transits to tight packing, the arrangement of particles has been changed. Thus, the contact force between particles and interaction forces between particles and the membrane will be enhanced so that the particles are not allowed to move. Thus the particles group shows a solid-like state and the jamming forms. Usually, the traditional method uses the pneumatic system to achieve the particle-jamming effect. As shown in Figs. 1(*a*) and 1(*b*), when vacuum pressure is applied, the particles jam each other firmly under vacuum pressure. Furthermore, the increasing interaction forces lock the particles, resulting in high stiffness [31]. Another way to achieve the jamming effect is using smart deformable particles or membranes. First, as shown in Fig. 1(*c*), different types of particles are filled in the chamber, and some of the particles are made of smart materials which can achieve active behaviors of expansion or deformation by external stimuli, such as temperature or humidity. After the active behaviors, the arrangement of particles and the total volume of the particle group will change, then the elastic membrane will lock the particles and form jamming. Then, as shown in Fig. 1(*d*), using the shrinking membrane is another option. In this case, particles are still rigid, but the membrane is made of smart material with a shrinkage coefficient. During the shrinking process, the particles will interact with the deformable membrane and jam each other until the extreme state. In the extreme state, particles can also be locked by the shrinking membrane to form a tight packing state, resulting in the jamming effect.

Based on the particle-jamming effect, various soft membrane-wrapped containers are designed to improve performance when grasping irregular and heavy objects [32–34]. To further improve the performance of the soft grippers, the method which combines the particles with a pneumatic driver has also been proposed to enhance the contact force. Based on the combination method, a variable stiffness gripper with particles and air cavities is designed to increase the structure stiffness using the particle-jamming effect [35]. A particle transmission method based on the pneumatics actuator is proposed for soft gripper design. The bending of the actuator is achieved by using the pneumatic actuator, and its stiffness is increased accordingly by controlling the volume of particles injected into the elastic chamber [26]. However, the interaction between particles and covered surfaces will counteract the actuator, limiting the grippers' bending range.

The research on soft robotics is mainly based on experiments, which usually require many resources. However, with the developments in computational technology, numerical simulations bring possibilities for developing soft robotics. Wang et al. proposed a new type of soft machine driven by buckling actuators based on numerical simulation. As a result, the critical design parameters in soft machines were explored, which were typically difficult to obtain in experiments [36]. Coevoet et al. designed a locomotion and manipulation control method for soft structure, which's application possibilities were verified in various physical scenarios using numerical analysis [37]. Furthermore, Dilibal et al. used numerical analysis to design a soft gripper with integrated soft force sensors. In the meantime, the grasping capability of the manufactured gripper was experimentally evaluated by changing the pneumatic pressure [38]. It is shown that the numerical simulation method can cover the shortages in the experiments and realize the optimal design of soft robotics with high efficiency.

This study proposes a novel deformable actuator based on the particle-jamming effect. The contributions of the proposed research are summarized in several points. First, the design is a dual-chambers structure that uses rigid and deformable particles combined with the flexible membrane as carriers. The dual-chambers actuator can achieve large bending deformation by membrane

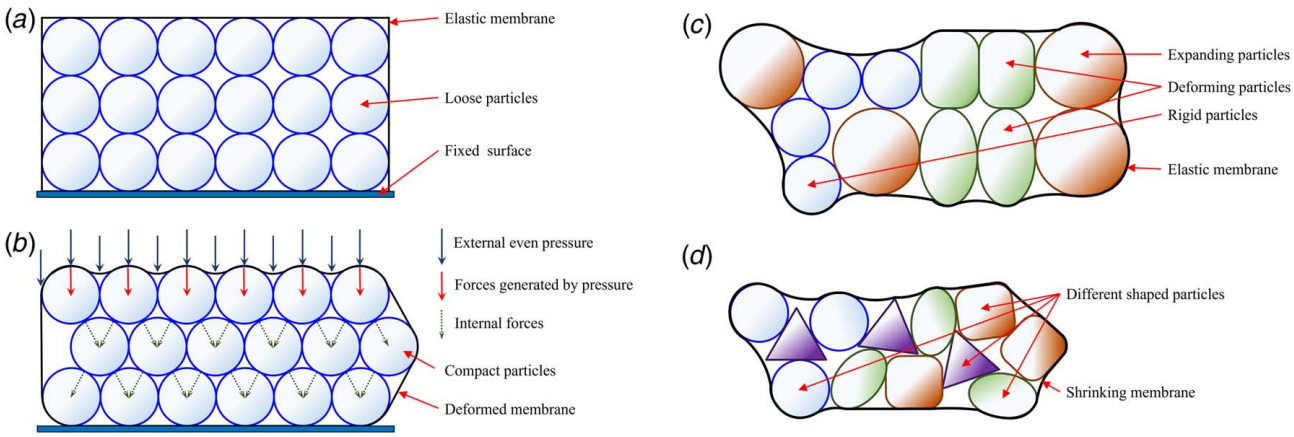

Fig. 1 Rigid particle-jamming effect and smart particle-jamming effect: (*a*) before jamming, (*b*) after jamming, (*c*) chamber with expanding and deforming particles, and (*d*) chamber with shrinking membrane

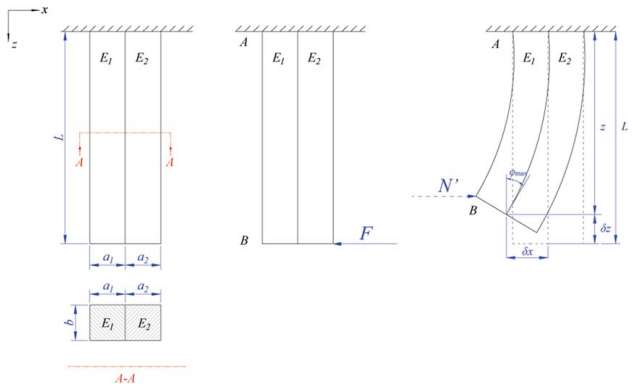

Fig. 2 The cantilever beam of length *L*

shrinking or particles expanding, and different bending behaviors can be achieved by controlling the design parameters including particle diameter ratio, actuator length, and material property. Compared with traditional pneumatic and single-chamber particle-jamming actuators, the proposed concept design can improve the bending angle and bending stiffness significantly. Furthermore, a bidirectional discrete element method-finite element method (DEM-FEM) coupling numerical model is presented to analyze the load and the deformation of the elastic chamber interacted by particles, which brings a novel approach to characterize the motion and stiffness of the particle jamming-based actuators.

2 Conceptual Design

2.1 Theoretical Background. The proposed actuator is inspired by the bender configuration of active compliant structures [39–42]. The bending curvature of a large deflection bender modular is shown in Fig. 2. The δ_x and δ_z are the horizontal and vertical displacements at the free end, respectively, and φ_{max} refers to the maximum slope of the bender. It is assumed that the length of the middle layer between the two parts of the bender always remains the same.

If the right part of the bender with the elastic modulus E_1 has a maximum expansion of Δl, the maximum curvature $1/\rho$ of the bender can be described as

$$\frac{1}{\rho}=\frac{\Delta l}{\frac{a_1+a_2}{2}+\frac{2(E_1I_1+E_2I_2)}{a_1+a_2}\left(\frac{1}{E_1a_1}+\frac{1}{E_2a_2}\right)} \tag{1}$$

Thus, the equivalent external force F can be described as

$$F=\frac{1}{\rho}\left(\frac{2}{(a_1+a_2)a_1}(E_1I_1+E_2I_2)+\frac{E_1a_1}{2}\right) \tag{2}$$

In addition, $\varphi_{max}=180L/\pi\rho$, and consider the bender as a whole and the equivalent elastic modulus $\bar{E}$ and the equivalent moment of inertia $\bar{I}$, the x and z coordinates of the horizontal and vertical deflections at any point along the neutral axis of the bender are found as follows:

$$z=\left|\sqrt{\frac{2\bar{E}\bar{I}}{F}}\left(\sqrt{\sin\varphi_{max}}-\sqrt{\sin\varphi_{max}-\sin\varphi}\right)\right| \tag{3}$$

$$x=\left|\sqrt{\frac{\bar{E}\bar{I}}{2F}}\int_0^{\varphi}\frac{\sin\varphi d\varphi}{\sqrt{\sin\varphi_{max}-\sin\varphi}}\right| \tag{4}$$

$$\delta_x=x(\varphi_{max}),\quad \delta_z=L-z(\varphi_{max}) \tag{5}$$

It can be seen that φ_{max}, δ_x, and δ_z are affected by the beam's equivalent elastic module $\bar{E}$, the equivalent moment of inertia $\bar{I}$, and the bender length L.

Additionally, the bending stiffness of the actuator is represented as S_a, which can be described as

$$S_a=\frac{N'z'}{\varphi_{max}-\varphi'} \tag{6}$$

where N' is the external interaction when the actuator touching with objects, z' is the new vertical position point, and φ' is the bending angle affected by N'.

2.2 Actuator Design. To describe the bending behavior of the proposed gripper, the structure of the actuator is discussed. First, it is assumed that all the materials used in the actuator are incompressible and the effect of gravity is not considered. In order to draw the concept of smart elements with engineered particles, two strategies of driving modes are used in the conceptual design stage, which are called expansion mode and shrinkage mode, respectively. For the expansion mode, as shown in Fig. 3, the covered membrane is made of conventional elastic material. Here, the particles in the right chamber will expand actively with a certain expansion coefficient to deform the whole structure. For the shrinkage mode, as shown in Fig. 4, a reverse process by controlling the behaviors of the membrane is considered. Different-sized rigid particles are filled into different chambers in one element, while the covered membrane is set to shrink with a certain shrinking coefficient to deform the whole element.

Furthermore, to validate the feasibility of the proposed design, two experimental cases are conducted as proof of concept of both the expansion and shrinkage modes. The experiments with the actuator's expansion and shrinkage modes are illustrated in Figs. 5 and 6, respectively. In Fig. 5 (left), the same-sized rigid particles fill both chambers, which are covered by an Ecoflex-00-50 (Smooth-On Company, Macungie, PA) silicone membrane. Then, the bigger particles in the right are used instead of the initial ones to represent the expanding process. Now, the actuator structure bends toward the left after adding the particles in, providing

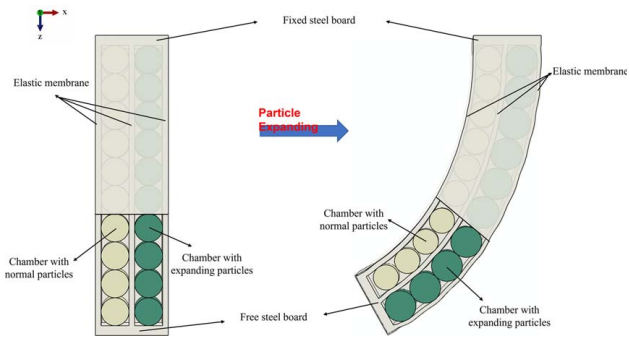

Fig. 3 Actuator working process of the expansion mode

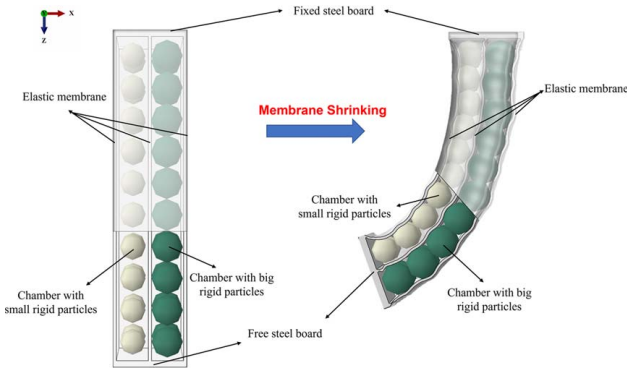

Fig. 4 Actuator working process of the shrinkage mode

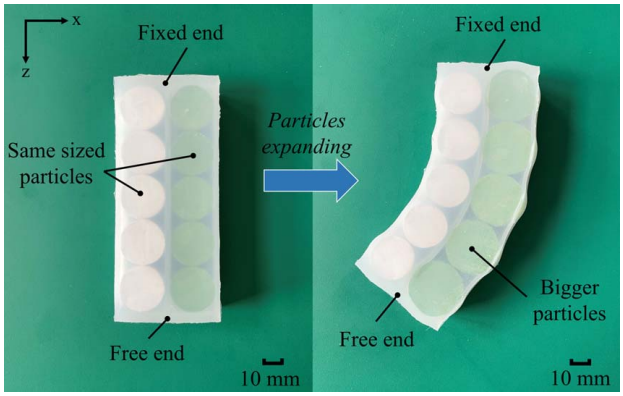

Fig. 5 The demonstration of the actuator of expansion mode

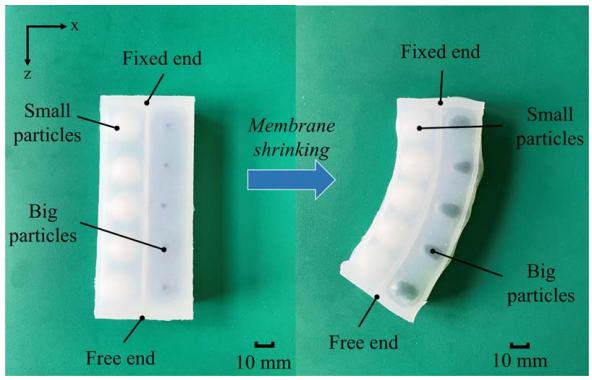

Fig. 6 The demonstration of the actuator of shrinkage mode

demonstrating proof of the principle of the expansion mode. Additionally, Fig. 6 demonstrates the shrinkage mode. First, the small rigid particles and big rigid particles are filled into the left chamber and right chamber, respectively. The total volume of the small particles is smaller than the volume of the chamber, thus the particles in the left chamber show a loose packing state in the beginning. Both chambers are covered by the silicone membrane. Then, as shown in Fig. 6 (right), the smaller chambers which have the same volume of small particles group are used instead to present the membrane shrinking process. The result demonstrates that the actuator bends toward the left, indicating that shrinkage mode can also achieve the actuator's bending. Moreover, the bending performance in these experimental cases will be used to compare and validate the simulation results in Sec. 4.1.1.

Additionally, as shown in Fig. 7, the geometric parameters of the actuator are defined as follows: the general structure has two chambers. The membrane at the length of L is fixed on the top and accessible at the end. The thicknesses at the top and the bottom are t_1, while the thicknesses of the outer membrane on both sides are t_0. It contains two layers with different widths a_1 and a_2. The two layers are connected by a thin film at a thickness of t_2 in between. Each chamber will be filled with particles with diameters of d_1 and d_2, respectively.

3 Methodology

The FEM-DEM coupling method is used for modeling. The FEM is used to accurately describe the deformations of the chamber due to (external) loads. Additionally, for the small amount of particles, DEM can describe the interactions at the particle level in granular materials with low computing resource consumption compared to traditional FEM. Besides, the FEM-DEM has already been

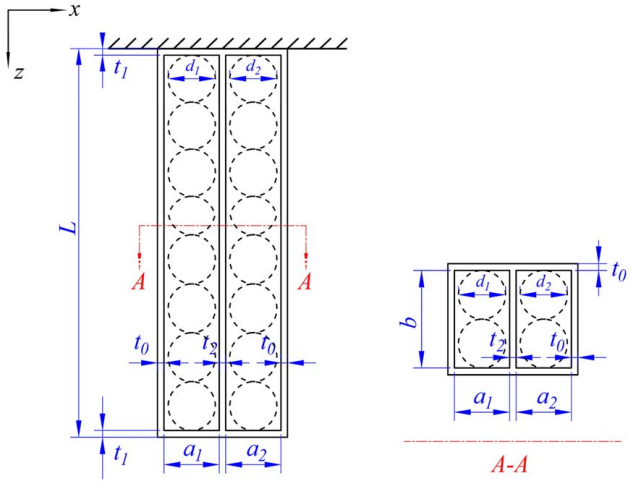

Fig. 7 A front view and the cross section view of the actuator structure

proven as a more efficient and realistic method to solve the interaction between rigid particles and elastic boundaries [43].

3.1 Numerical Model. Both the discrete elements and the finite element node motions are governed by Newton's second law. First, the external force F_i^{FEM} for finite element node i is given by

$$F_i^{\mathrm{FEM}} = m_i^{\mathrm{FEM}}\left(\frac{d^2 u_i^{\mathrm{FEM}}}{dt^2}\right) \tag{7}$$

where m_i^{FEM} is the mass of element i and u_i^{FEM} is the displacement of element i. And the total force F_i^{DEM} for discrete element node i, which composites of all collision force F_i^c, gravitational force F_i^g, and external force F_i^e, is given by

$$F_i^{\mathrm{DEM}} = F_i^c + F_i^g + F_i^e = m_i^{\mathrm{DEM}}\left(\frac{d^2 u_i^{\mathrm{DEM}}}{dt^2}\right) \tag{8}$$

where m_i^{DEM} is the mass of individual particle i and u_i^{DEM} is the displacement of discrete element i. In addition, the centroidal moment of element i of the discrete element i is given by [44]

$$M_i = I_i\left(\frac{d^2\theta_i}{dt^2}\right) \tag{9}$$

where I_i is the inertia moment of element i and θ_i is the rotation angle of element i. Equations (7)–(9) are solved using an explicit finite difference method based on the commercial platform ABAQUS.

Contact detection is necessary to calculate the interaction forces among the elements. The C-grid method is applied for the contact detection of the elements [45]. Besides, the node-to-surface method consists of a global search. Local search is used as the contact detection between the spherical discrete elements and the hexahedron finite meshes [46]. In this method, the discrete elements are regarded as the slave nodes, and the contact surfaces of the finite elements are regarded as the master surfaces. Global research determines the potential contact pairs, and the local search calculates the penetration value between the contact pairs. The interaction forces among the elements strongly depend on the contact model between contact pairs. The contacts of particle-to-particle and particle-to-surface are shown in Fig. 8. The overlap between discrete elements and discrete and finite elements, which represents the small deformation of the discrete element, is δ_{ij}. Moreover, the linear velocities and angular velocities of elements i and j are v_i, v_j, ω_i, and ω_j, respectively. It needs to be noted that there is no angular velocity in the finite elements.

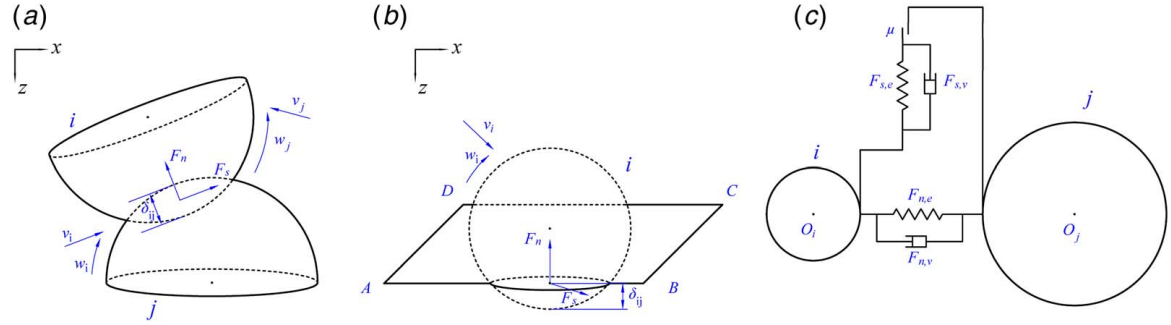

Fig. 8 Schematic of contact interaction and contact force of particles and wall surface: (*a*) the overlap between two particles, (*b*) the overlap between particle and the wall surface, and (*c*) the contact with spring, damper in both tangential and normal directions as well as sliding contact

The normal force F_n and the tangential force F_s can be written as

$$F_n = F_{n,e} + F_{n,\nu} \tag{10}$$

$$F_s = \begin{cases} F_{s,e} + F_{s,\nu} & |F_s| < f|F_n| \\ fF_n & |F_s| \geq f|F_n| \end{cases} \tag{11}$$

where $F_{n,e}$, and $F_{n,\nu}$ represent the normal spring force and the normal damping force, respectively; $F_{s,e}$ and $F_{s,\nu}$ represent the tangential spring force and tangential damping force, respectively. The friction coefficient is shown as f. The $F_{n,e}$, $F_{n,\nu}$, $F_{s,e}$, and $F_{s,\nu}$ can be calculated by Hertz–Mindlin theory [47]. Specially, there is an assumption that finite elements are regarded as spheres with infinite radii [48]. The $F_{n,e}$ and $F_{s,e}$ are shown as

$$F_{n,e} = \frac{4}{3} E^* \sqrt{R^*} \delta_{ij}^{\frac{3}{2}} \tag{12}$$

$$F_{s,e} = \frac{16}{3} G^* \sqrt{R^* \delta_{ij}^{\frac{3}{2}}} |u^*| \tag{13}$$

where R^* is the equivalent radius of the contact elements, which can be obtained by $R^* = (r_1 r_2)/(r_1 + r_2)$; the E^* and G^* are the relative elastic modulus and shear modulus, which can be illustrated as

$$\frac{1}{E^*} = \frac{1 - \upsilon_i^2}{E_i} + \frac{1 - \upsilon_j^2}{E_j} \tag{14}$$

$$\frac{1}{G^*} = \frac{2 - \upsilon_i^2}{G_i} + \frac{2 - \upsilon_j^2}{G_j} \tag{15}$$

where E_i, E_j, G_i, G_j, υ_i, and υ_j are the elastics modulus, shear modulus, and Poisson's ratios of elements i and j, respectively; and u^* is the relative displacement in the tangential direction which can be calculated by

$$u^* = \int_0^t v_{s,ij} dt \tag{16}$$

The $F_{n,\nu}$ and $F_{s,\nu}$ are shown as

$$F_{n,\nu} = -\frac{\Phi_n m_i m_j}{m_i + m_j} \cdot v_{n,ij} \tag{17}$$

$$F_{s,\nu} = -\frac{\Phi_s m_i m_j}{m_i + m_j} \cdot v_{s,ij} \tag{18}$$

where Φ_n and Φ_s represent the damping factors of normal and tangential directions; $v_{n,ij}$ and $v_{s,ij}$ represent the relative velocities of the normal and tangential directions.

3.2 Coupling Strategy. The coupling strategy is shown in Fig. 9. First, the mesh file containing the actual triangulated surface elements and the number of the original finite element (FE) elements are used as input into the DEM solver as a wall condition [43]. Then, the DEM solver calculates particles' interaction forces, displacements, and velocities in a specific DEM time-step. The next step is calculating the node forces based on the particle load and then transferring them into each FEM element. Furthermore, the node forces must be transferred to a distributed load to interpolate them onto each FE element. Consequently, the deformations of mesh elements and displacements of nodes can be calculated. The deformed mesh will update the old grid information to the DEM solver, which is a complete coupling FEM time-step which is a multitude (default value, 10) of the minor DEM time-step.

3.3 Simulation Setup

3.3.1 Simulation Implementation. In the shrinkage mode, the membrane is set to finite element units and the particles are established by DEM. However, in expansion mode, both the membrane and particles are set to finite element units. The structured mesh is used to establish the finite element units, and after mesh convergence analysis, the hexahedral mesh is selected and the mesh numbers are set to 92,267 and 3657 for membrane and particles in expansion mode. Besides, the Noe–Hookean model is used as the constitutive model to characterize the mechanical property of

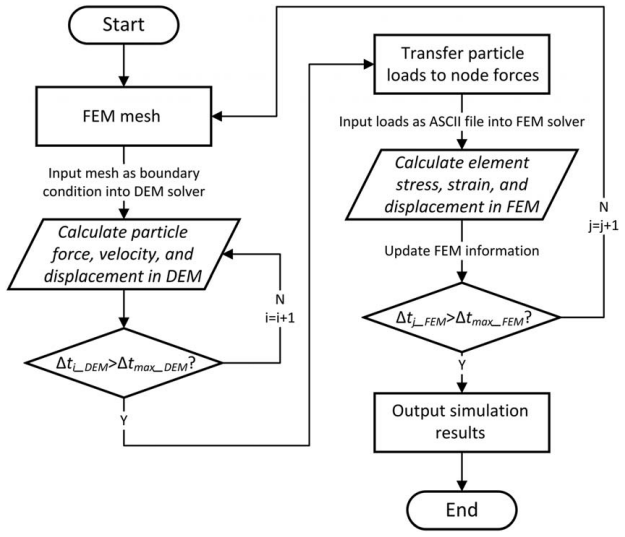

Fig. 9 Schematic of coupling strategy

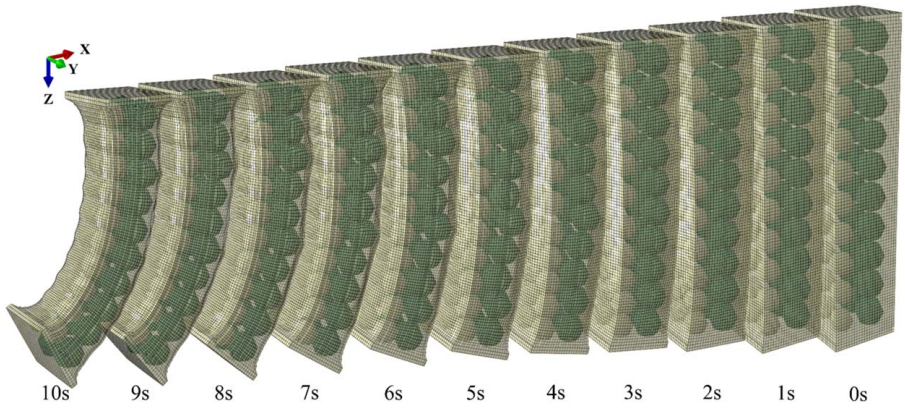

Fig. 10 The bending process as a function of time with membrane shrinking mode

the membrane made of Ecoflex-00-50. The fitted parameters of μ, denoting the coefficient depending on the material property, are given by $\mu = 0.0481$ [49]. In order to achieve the shrinking process, the membrane material was set thermos-sensitive with a constant shrinking rate coefficient $\gamma = -0.01$, which is triggered by temperature increase. Furthermore, as for the expansion mode, the membrane is set as normal elastic material without any thermal response. Instead, the filling particles are thermos-sensitive, with an expansion coefficient of $\alpha = 0.01$. The membrane shrinking strain ε_s, and particle expansion strain ε_e can be described as

$$\varepsilon_s = \gamma(T_1 - T_0) \cdot t \tag{19}$$

$$\varepsilon_e = \alpha(T_1 - T_0) \cdot t \tag{20}$$

where T_0 is the initial temperature with a constant value of 300 K, T_1 is the operating temperature which is set to 330 K, t represents the total simulation time, 10 s. And for both simulations, the time-step is set to constant with $\Delta t = 10^{-6}$ s.

As an example, the shrinking process of a total simulation time is shown in Fig. 10, the overall structure bends toward the layer of small particles with the shrinking of the membrane. In the initial stage, the elastic membrane covering the particles assumes a cubic structure. During the working phase, the membrane shrinks and interacts with particles continuously over time, and the difference in particle sizes in the two chambers causes the different shrinking extents, which eventually results in bending.

3.3.2 Case Study. As shown in Fig. 11, the bending performance of the proposed actuator is indicated by bending angle and deflections. The δ_x and δ_z are the horizontal and vertical displacements at the free end, respectively. The $\varphi_{\max}$ refers to the maximum slope of the actuator element.

Additionally, considering different independent influential parameters, variable simulation cases were conducted as the sensitivity analysis to investigate the behaviors of the proposed actuator. The first set of simulations investigates how particle size differences influence the actuator's behaviors. The second set of simulations explores how the major structural parameters influence the actuator's behaviors. The last set of simulations investigates how the membrane's material property influences the soft actuator's behaviors. It should be noted in the last set of simulations, the linear model is used instead of the hyperelastic model in the simulations for analyzing the effects of materials with an extensive range of stiffness on the bending performance. Thus, all materials are assumed to be with a fixed elastic modulus. Besides, different driving modes of the actuator are also compared. The specific actuator parameters are shown in Table 1, and the material's properties are shown in Table 2.

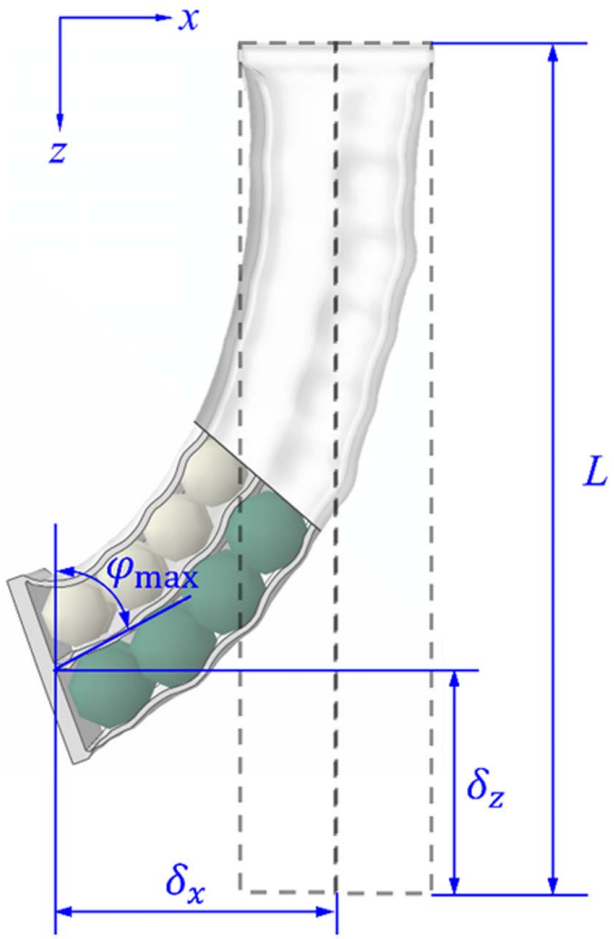

Fig. 11 The illustration of the bending angle and deflection of the actuator

Table 1 Actuator parameters

Driving modes	Particle diameter ratio β_{ls}	Actuator length L (mm)	Other sizes (mm)
Shrinkage mode Expansion mode	1–2	28–448	$a_1 = a_2 = 20$ $t_0 = t_2 = 2$ $t_1 = 4$ $b = 40$

Table 2 Materials properties

	Particles	Membrane	End board
Density (kg/m^2)	$\rho_p = 1180$	$\rho_m = 950$	$\rho_b = 7800$
Elastic modulus (MPa)	$E_p = 2910$	$E_m = 50 \sim 60{,}000$	$E_b = 2{,}10{,}000$
Poisson's ratio	$\nu_p = 0.38$	$\nu_m = 0.48$	$\nu_b = 0.32$

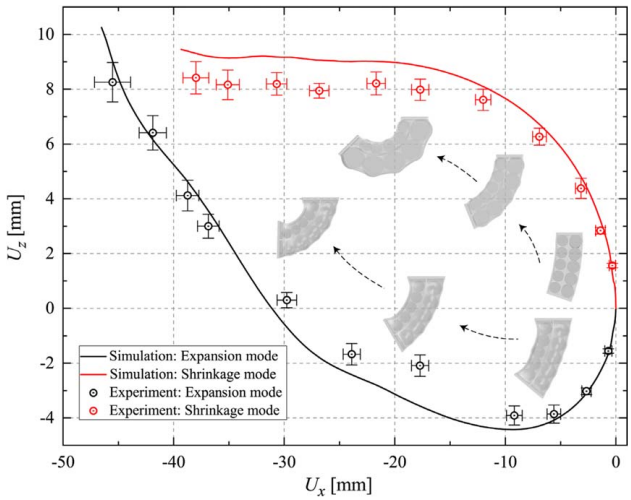

Fig. 12 The displacements in the *x*-direction and *z*-direction of simulation results and experimental results of the proposed novel actuator

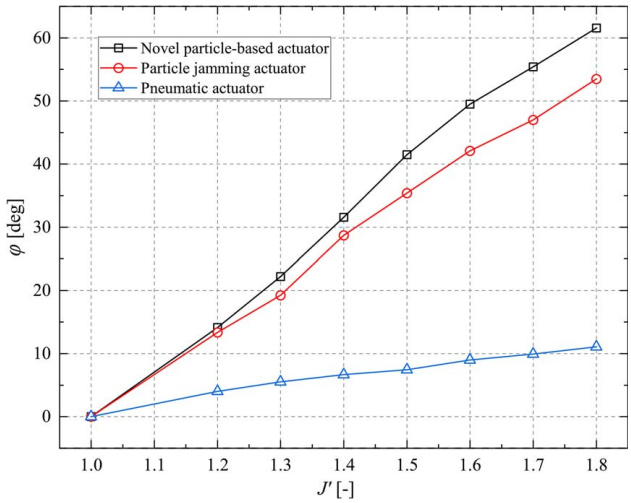

Fig. 13 The bending angle comparison of the proposed design and the research by Li et al. [26]

4 Results and Discussion

4.1 Comparison of the Bending Performances and Driving Modes

4.1.1 Validation and Comparison of the Bending Performance. To validate the bending performances of the designed actuator, the detailed results of experiments and simulations relating to the configuration in Sec. 2.2 are compared. As for the experimental cases, the reference point at the actuator's free end (cf. Fig. 11) is selected to describe the displacements. Besides, the coordinate paper is used to quantify the motion range of the actuator, and the displacements are measured by counting the girds step by step. The displacements in the *x*-direction and

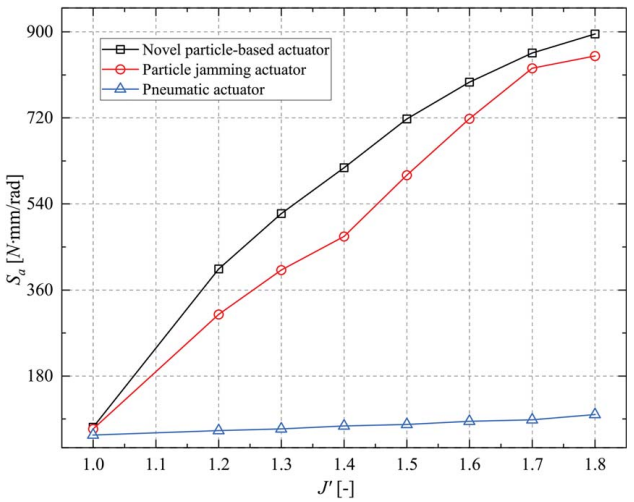

Fig. 14 The bending stiffness comparison of the proposed design and the research by Li et al. [26]

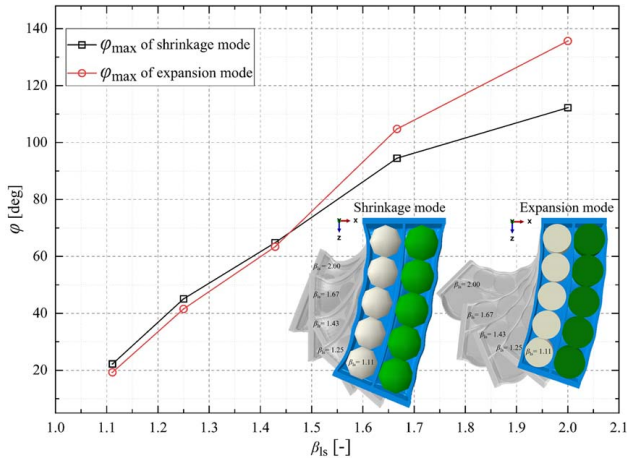

Fig. 15 Comparison of bending angles of different driving modes with different β_{ls}

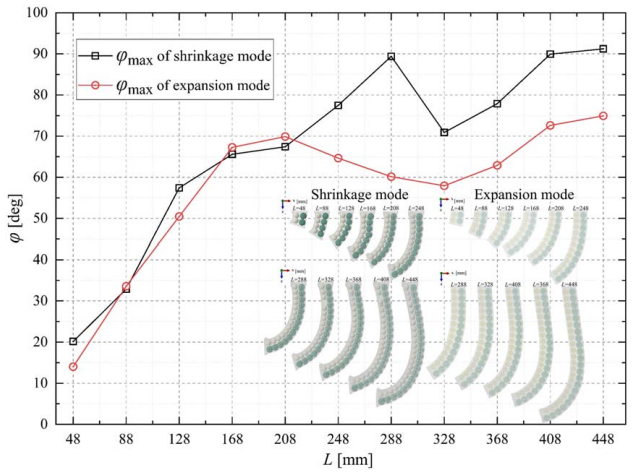

Fig. 16 Comparison of different driving modes of different actuator lengths *L*

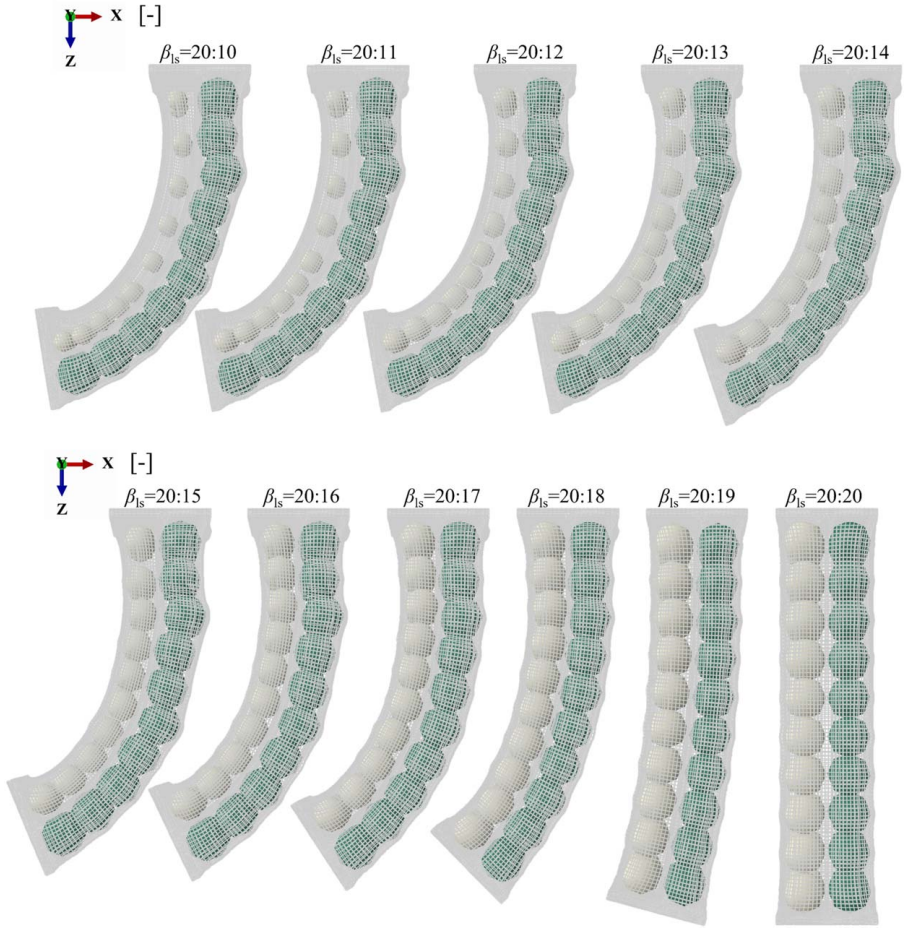

Fig. 17 The actuator bending performance of different β_{ls}

z-direction are represented as U_x and U_z, respectively. The results are shown in Fig. 12, the error bars are the displacement differences of the experimental cases which are tested three times. In addition, the coordinate origin represents the initial state, and bending process is shown as the configuration shown in Fig. 12. The simulation results show good consistency with the experimental case results in the moving displacement at the free end, further proving the feasibility of the design.

Furthermore, the bending angle and the stiffness of the shrinkage mode are compared with pneumatic and single-chamber particle-jamming actuators to evaluate the design concept [26]. The parameter J' represents the volume ratio between the cavity (with smaller particles) before and after shrinkage, and for other actuators, J' is the volume ratio between the bending state and the initial state. Essentially, J' is the volume difference before and after deformation. As shown in Fig. 13, the bending angle of all actuators increases as the volume ratio increases. Compared with the pneumatic actuator, the bending angle of our proposed particle-based actuator increases more sharply and exhibits a maximum six-fold increase. Compared with the particle-jamming actuator, the trend of the bending angle change is similar, however, our design can obtain an extra 8 deg bending angle at the maximum volume ratio. As shown in Fig. 14, the bending stiffness of our design and the particle-jamming actuator increases sharply as the volume ratio increases, but the bending stiffness of the pneumatic actuator changes very less. Compared with the pneumatic actuator, the bending stiffness of our design exhibits a maximum nine-fold increase. Compared with the particle-jamming actuator, the trend of the bending stiffness change is also similar, but our design exhibits greater stiffness across the range of volume ratio from 1.2 to 1.8.

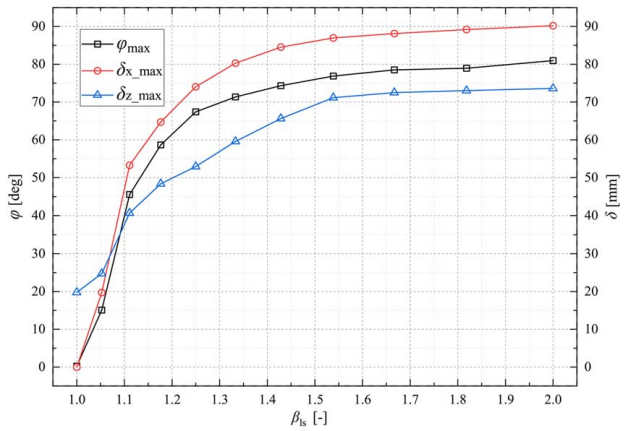

Fig. 18 The actuator bending angle and deflection curves of different β_{ls}

4.1.2 Comparison of the Shrinkage Mode and Expansion Mode. The bending performances of different driving modes are compared in this section. The bending performances of different β_{ls} actuated by different driving modes are compared in Fig. 15. Generally, the shrinkage mode and the expansion mode show good agreement in the bending curvature. Individually, the angle difference between the two driving modes rises gradually as β_{ls} increase, but the maximum difference value is only up to 30 deg.

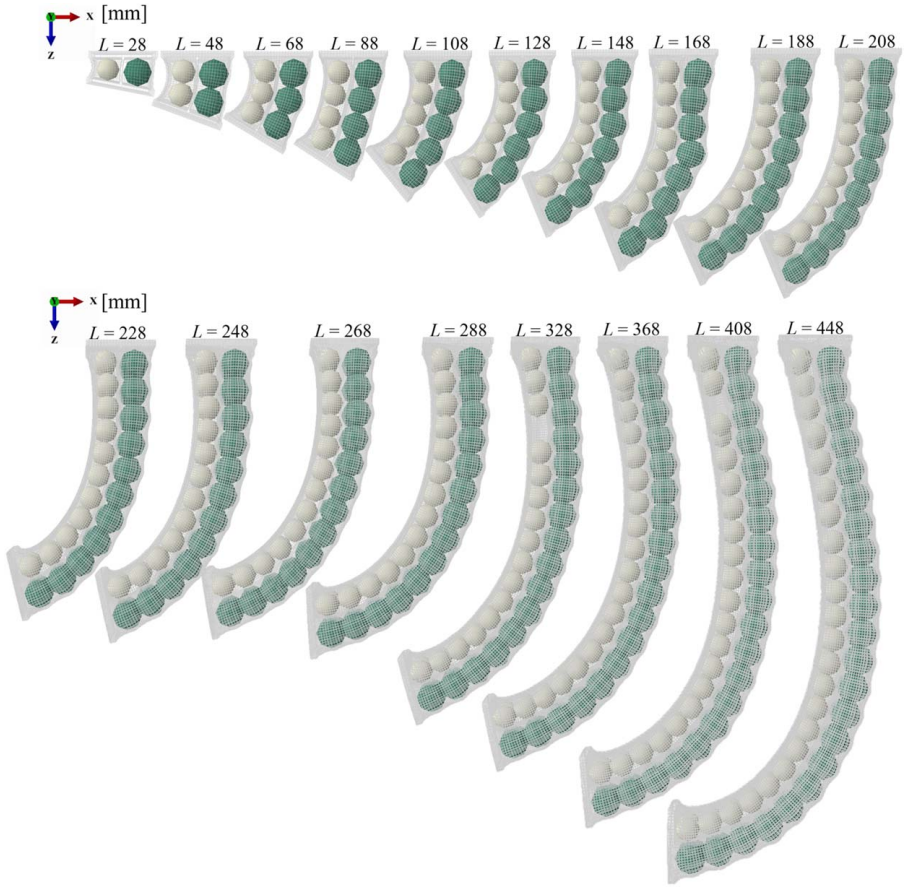

Fig. 19 The finial bending state of the actuator of different *L*

To further explore whether expansion and shrinkage modes can achieve similar bending performance, as shown in Fig. 16, the effects of the actuator length on the bending performance of different driving modes are analyzed. First, both driving modes' bending angle curves increase gradually, dropping within a specific range of L and then going up again until L comes to 448 mm. Specifically, both driving modes show a similar bending trend at the beginning of L from 48 mm to 208 mm. When the length increases over 208 mm, the bending angle of the expansion mode starts to drop, but the bending angle of the shrinkage mode keeps rising. In addition, when L comes to 288 mm, the bending angle of shrinkage mode also starts to drop, and the bending angle curve of expansion and shrinkage modes shows a similar trend again after L reaches 325 mm. Therefore, although the bending angles of shrinkage and expansion mode differ when L is over 248 mm, both the expansion mode and shrinkage mode of the actuator can achieve the desired design.

4.2 Effect of the Particle Diameter Ratio. In this section, the effects of the diameter ratios of particles in the two chambers on the bending angle and deflection are analyzed. As shown in Fig. 17, in general, the final bending state of the membrane shows a significant difference of β_{ls} from 1 to 1.33, while the final bending presents an imperceptible difference of β_{ls} from 1.33 to 2. Specifically, as shown in Fig. 18, the difference in bending angle φ is up to 50 deg of β_{ls} from 1.1 to 1.33 but only 10 deg of β_{ls} from 1.33 to 2. As for the deflection change, the maximum deflection δ_{x_max} and δ_{z_max} climb gradually of β_{ls} from 1.1 to 1.33 and remain between 55 mm and 65 mm of β_{ls} from 1.1 to 1.33.

Generally, the membrane shrinkage induces the volume difference between two chambers, resulting in the bending. Specifically, when β_{ls} is at a relatively low level, both large or small particles group will reach the tight packing state before the chamber gets into the shrinking limit. At this time, the volume difference is mainly between the large particle group and the tiny particles group. Thus, the bending angle and deflections are variable as the β_{ls} change. Additionally, when the value of β_{ls} gets larger, the volume of the particles group in the left cannot form the tight packing state before the chamber reaches the shrinking limit, which means the particles in the left chamber will not take the main effects anymore. Thus, the bending state is stable when β_{ls} is up to a high level from 1.33 to 2.

4.3 Effect of the Actuator Length. In this section, the effect of the actuator length on the bending angle and deflection is

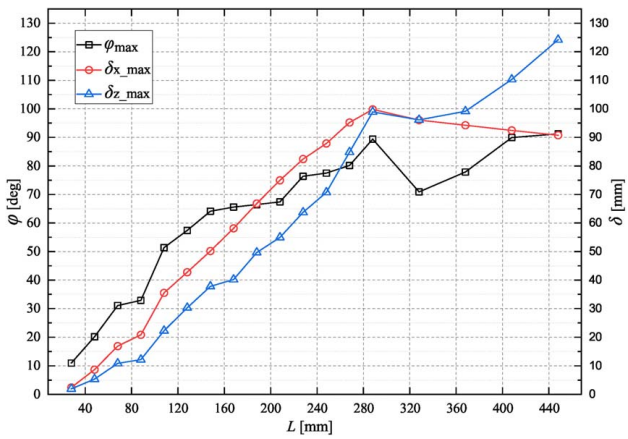

Fig. 20 The bending angle and the deflection curve of the actuator of different *L*

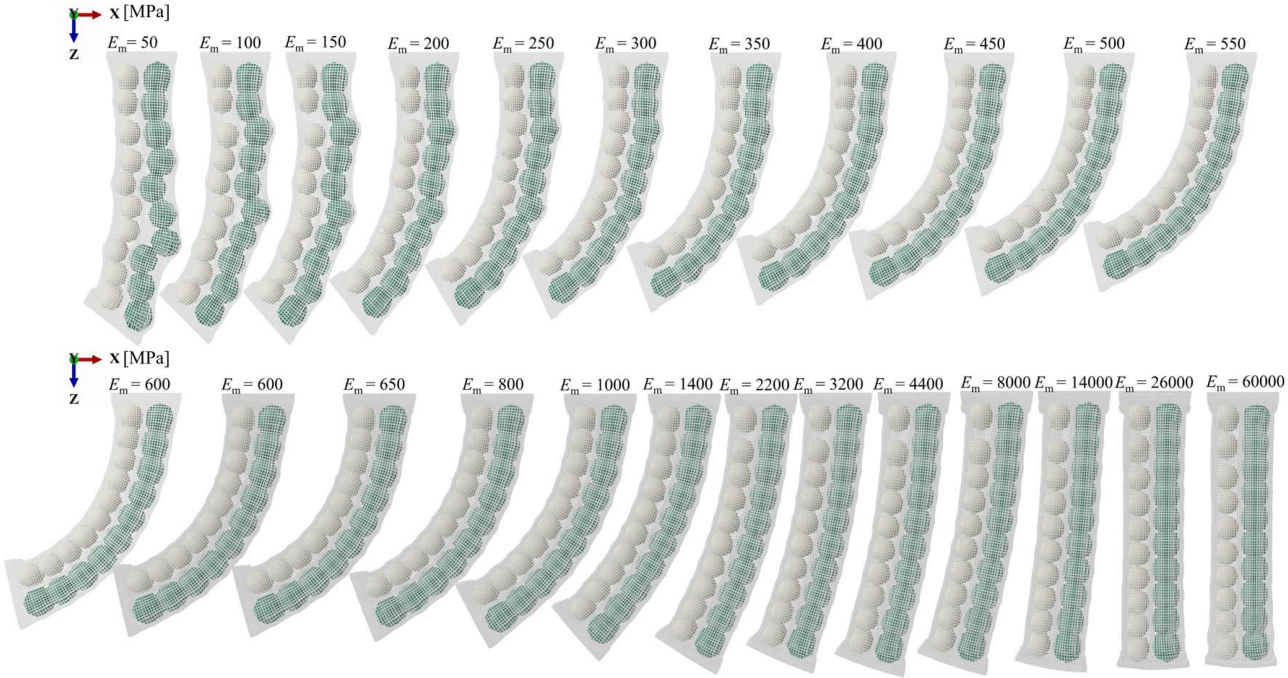

Fig. 21 The final bending state of the actuator for different E_m

analyzed. The variation of the whole actuator length depends on the chamber length and particle number, thus the particle number also changes in exploring the effect of actuator length. The results of the final bending state of different actuator lengths from 28 mm to 448 mm are shown in Fig. 19. First, the final bending angle increases gradually of L from 28 mm to 288 mm, while the final bending angle first drops when L comes to 328 mm and then goes up until L comes to 448 mm. Then, when L is over 288 mm, the overall structure exhibits a curvature near the fixed end rather than only at the free end. This phenomenon can be explained by transitioning from a bending state to a curling state. First, when the actuator length L is at a low level, the internal force produced by the interactions between particles and membrane only takes effect on the structure in the horizontal direction, thus the bending state forms. However, when the actuator length L comes to a high level, the internal force produced by the interactions between particles begins to take effect in the vertical direction, which causes the curling state.

Additionally, to observe the deformation trend specifically, the bending angle φ and the deflection δ at the free end are illustrated in Fig. 20. A similar changing trend of bending angle shows up, the δ_{x_max} and δ_{z_max} drop of L from 288 mm to 328 mm. When the actuator length is from 328 mm to 448 mm, δ_{x_max} keeps decreasing while δ_{z_max} climbs again. This indicates that, first when curvature changes from a bending state to a curling state, the effect of particles interacting on the membrane gradually weakens, thereby reducing the horizontal deflections of the actuator. Then, as for δ_{z_max}, it decreases transitorily in the transition state, and then owing to the effects of the shrinking membrane and interactions of particles to particles and particles to the membrane, δ_{z_max} shows a rising trend of the curling state of actuator length from 288 mm to 328 mm.

4.4 Effect of the Membrane Material Property. In this section, the effects of the membrane material property on the bending angles and deflections are analyzed. The bending performance is shown in Fig. 21. Generally, the bending angle increases gradually with the E_m increasing until around 650 MPa and then drops off when E_m reaches 60,000 MPa. In addition, the arrangement of the particles in each chamber is more ordered as the membrane is stiffer. The phenomenon of the bending angle increasing can be explained as the changes in the relationship between stress and strain. When the membrane material is of a low-level elastic modulus, the membrane is easy to deform with lower stress, and the structure is too soft to support a bending curvature, thus, little bending happens. Also, when the membrane material becomes much stiffer, the particles become softer compared to the membrane, thus, there are fewer interaction effects caused by particles on the membrane to achieve a bending behavior. Therefore, the bending angle no longer increases but drops down.

Furthermore, the bending angle and the deflection at the free end of different membrane materials are illustrated in Fig. 22. The bending angle increases gradually as the E_m increases from 50 MPa to 600 MPa and then drops down as the E_m changes from 600 MPa to 60,000 MPa. The deflection change has a similar trend to the bending angle variation. In addition, it can be seen that δ_{z_max} remains around 30 mm rather than keeps going down when the elastic modulus of the membrane changes from 8000 MPa to 6000 MPa, which also indicates that the interactions between membrane and particles no longer contribute to bending when the membrane is stiff enough, thus the overall structure becomes a hard shell with a fixed shrinking coefficient.

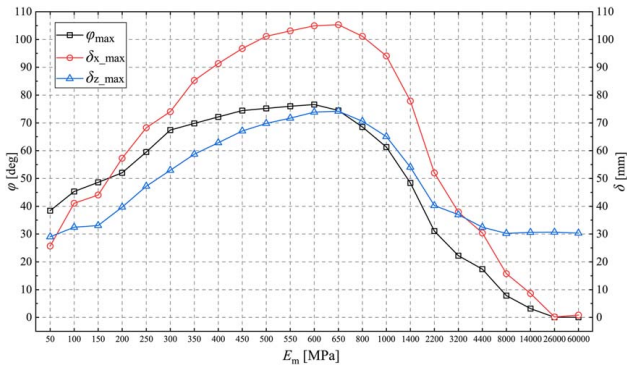

Fig. 22 The bending angle (include symbol) and the deflection (include symbol) of the actuator as a function of E_m

5 Conclusions

The soft gripper is endowed with flexibility in grasping irregularly shaped and fragile objects. However, the challenge of trading off the large deformation and stiffness variation limits the scope of applications of current soft gripper actuators. To achieve large deformation and stiffness variation, this study proposed a novel conceptual design of a particle-based soft gripper actuator. The soft actuator based on the differential driving modes mechanism is characterized by a dual-deformable chamber structure filled with tailored particles. The dual-deformable chamber structure supports the large deformation behavior, and the particle-jamming effect is used to achieve the stiffness variation. Moreover, numerical methods were developed to quantify the relationships between the design parameters, the bending angle, and the deflection.

The simulation results are in good agreement with the experimental cases, which have validated the feasibility of the simulation method. In addition, compared with pneumatic actuators and single-chamber particle-jamming actuators, the proposed design can achieve larger deformations and exhibit higher bending stiffness. Thus, the proposed concept can develop to handle objects of large scale and weight or arbitrary shapes, such as windmill blades and submarine pipes. Furthermore, the specific results have shown that both the shrinkage mode and expansion mode of the actuator can achieve the bending behaviors of different particle diameter ratios from 1 to 2 and different actuator lengths from 48 mm to 448 mm. In addition, the larger bending angle and more significant deflection can be achieved by increasing the particle diameter ratio from 1 to 2, the actuator length from 28 mm to 288 mm, and the elastic modulus of the membrane from 50 MPa to 600 MPa. However, when the actuator length increases from 288 mm to 448 mm and the elastic modulus of the membrane from 600 MPa to 60,000 MPa, the performance of the soft actuator will deteriorate.

The proposed conceptual design will support completing the design, modeling, and fabrication of a soft-grasping gripper to achieve potential applications in the large-scale scene. Specifically, the modeling of the particles or the membrane, which are made of engineered smart material, will be conducted to achieve the prominent deformation behaviors of the gripper actuator with the active process.

Acknowledgment

This work is supported by the National Natural Science Foundation of China Grant No. 52071240, the Higher Education Discipline Innovation Project Grant No. BP0820028, and China Scholarship Council Grant No. 202006950011. The financial contributions are gratefully acknowledged.

Conflict of Interest

The authors declare that they have no known competing financial interests or personal relationships that could have appeared to influence the work reported in this paper.

Data Availability Statement

The authors attest that all data for this study are included in the paper.

References

[1] Krüger, J., Lien, T. K., and Verl, A., 2009, "Cooperation of Human and Machines in Assembly Lines," CIRP Ann., **58**(2), pp. 628–646.

[2] Bertelsen, A., Melo, J., Sánchez, E., and Borro, D., 2013, "A Review of Surgical Robots for Spinal Interventions," Int. J. Med. Rob. Comput. Assist. Surg., **9**(4), pp. 407–422.

[3] Hirzinger, G., Brunner, B., Landzettel, K., and Schott, J., 1998, "Preparing a New Generation of Space Robots—A Survey of Research at DLR," Rob. Auton. Syst., **23**(1–2), pp. 99–106.

[4] Okamura, A. M., Smaby, N., and Cutkosky, M. R., 2000, "An Overview of Dexterous Manipulation," IEEE International Conference on Robotics and Automation, Symposia Proceedings, San Francisco, CA, Apr. 24–28, pp. 255–262.

[5] Xydas, N., Bhagavat, M., and Kao, I., 2000, "Study of Soft-Finger Contact Mechanics Using Finite Elements Analysis and Experiments," Proceedings 2000 ICRA. Millennium Conference, IEEE International Conference on Robotics and Automation, Symposia Proceedings, San Francisco, CA, Apr. 24–28, pp. 2179–2184.

[6] Walker, J., Zidek, T., Harbel, C., Yoon, S., Strickland, F. S., Kumar, S., and Shin, M., 2020, "Soft Robotics: A Review of Recent Developments of Pneumatic Soft Actuators," Actuators, **9**(1), p. 3.

[7] Rus, D., and Tolley, M. T., 2015, "Design, Fabrication and Control of Soft Robots," Nature, **521**(7553), pp. 467–475.

[8] Cho, K.-J., Koh, J.-S., Kim, S., Chu, W.-S., Hong, Y., and Ahn, S.-H., 2009, "Review of Manufacturing Processes for Soft Biomimetic Robots," Int. J. Precis. Eng. Manuf., **10**(3), pp. 171–181.

[9] Coevoet, E., Morales-Bieze, T., Largilliere, F., Zhang, Z., Thieffry, M., Sanz-Lopez, M., Carrez, B., Marchal, D., Goury, O., and Dequidt, J., 2017, "Software Toolkit for Modeling, Simulation, and Control of Soft Robots," Adv. Rob., **31**(22), pp. 1208–1224.

[10] Gupta, U., Qin, L., Wang, Y., Godaba, H., and Zhu, J., 2019, "Soft Robots Based on Dielectric Elastomer Actuators: A Review," Smart Mater. Struct., **28**(10), p. 103002.

[11] Li, X., Zhang, Z., Sun, M., Wu, H., Zhou, Y., Wu, H., and Jiang, S., 2020, "A Magneto-Active Soft Gripper With Adaptive and Controllable Motion," Smart Mater. Struct., **30**(1), p. 015024.

[12] Hamburg, E., Vunder, V., Johanson, U., Kaasik, F., and Aabloo, A., 2016, "Soft Shape-Adaptive Gripping Device Made From Artificial Muscle," Smart Materials and Nondestructive Evaluation for Energy Systems, Las Vegas, NV, Mar. 20–24, pp. 296–302.

[13] Wehner, M., Truby, R. L., Fitzgerald, D. J., Mosadegh, B., Whitesides, G. M., Lewis, J. A., and Wood, R. J., 2016, "An Integrated Design and Fabrication Strategy for Entirely Soft, Autonomous Robots," Nature, **536**(7617), pp. 451–455.

[14] Mosadegh, B., Polygerinos, P., Keplinger, C., Wennstedt, S., Shepherd, R. F., Gupta, U., Shim, J., Bertoldi, K., Walsh, C. J., and Whitesides, G. M., 2014, "Pneumatic Networks for Soft Robotics That Actuate Rapidly," Adv. Funct. Mater., **24**(15), pp. 2163–2170.

[15] Han, D., Farino, C., Yang, C., Scott, T., Browe, D., Choi, W., Freeman, J. W., and Lee, H., 2018, "Soft Robotic Manipulation and Locomotion With a 3D Printed Electroactive Hydrogel," ACS Appl. Mater. Interfaces, **10**(21), pp. 17512–17518.

[16] Pourazadi, S., Bui, H., and Menon, C., 2019, "Investigation on a Soft Grasping Gripper Based on Dielectric Elastomer Actuators," Smart Mater. Struct., **28**(3), p. 035009.

[17] Zhang, Z., Li, X., Yu, X., Chai, H., Li, Y., Wu, H., and Jiang, S., 2019, "Magnetic Actuation Bionic Robotic Gripper With Bistable Morphing Structure," Compos. Struct., **229**, p. 111422.

[18] Hager, M. D., Bode, S., Weber, C., and Schubert, U. S., 2015, "Shape Memory Polymers: Past, Present and Future Developments," Prog. Polym. Sci., **49**, pp. 3–33.

[19] Sun, L., Huang, W. M., Ding, Z., Zhao, Y., Wang, C. C., Purnawali, H., and Tang, C., 2012, "Stimulus-Responsive Shape Memory Materials: A Review," Mater. Des., **33**, pp. 577–640.

[20] Cianchetti, M., Licofonte, A., Follador, M., Rogai, F., and Laschi, C., 2014, "Bioinspired Soft Actuation System Using Shape Memory Alloys," Actuators, 3(3), pp. 226–244.

[21] Lendlein, A., and Gould, O. E., 2019, "Reprogrammable Recovery and Actuation Behaviour of Shape-Memory Polymers," Nat. Rev. Mater., **4**(2), pp. 116–133.

[22] Bartlett, N. W., Tolley, M. T., Overvelde, J. T., Weaver, J. C., Mosadegh, B., Bertoldi, K., Whitesides, G. M., and Wood, R. J., 2015, "A 3D-Printed, Functionally Graded Soft Robot Powered by Combustion," Science, **349**(6244), pp. 161–165.

[23] Shepherd, R. F., Ilievski, F., Choi, W., Morin, S. A., Stokes, A. A., Mazzeo, A. D., Chen, X., Wang, M., and Whitesides, G. M., 2011, "Multi-gait Soft Robot," Proc. Natl. Acad. Sci. U. S. A., **108**(51), pp. 20400–20403.

[24] Hao, Y., Gong, Z., Xie, Z., Guan, S., Yang, X., Ren, Z., Wang, T., and Wen, L., 2016, "Universal Soft Pneumatic Robotic Gripper With Variable Effective Length," 2016 35th Chinese Control Conference (CCC), Chengdu, China, July 27–29, pp. 6109–6114.

[25] Bishop-Moser, J., Krishnan, G., Kim, C., and Kota, S., 2012, "Design of Soft Robotic Actuators Using Fluid-Filled Fiber-Reinforced Elastomeric Enclosures in Parallel Combinations," 2012 IEEE/RSJ International Conference on Intelligent Robots and Systems, Vilamoura-Algarve, Portugal, Oct. 7–12, pp. 4264–4269.

[26] Li, Y., Chen, Y., Yang, Y., and Li, Y., 2019, "Soft Robotic Grippers Based on Particle Transmission," IEEE/ASME Trans. Mech., **24**(3), pp. 969–978.

[27] Udupa, G., Sreedharan, P., and Aditya, K., 2010, "Robotic Gripper Driven by Flexible Microactuator Based on an Innovative Technique," 2010 IEEE Workshop on Advanced Robotics and Its Social Impacts, Seoul, South Korea, Oct. 26–28, pp. 111–116.

[28] Walker, I. D., Dawson, D. M., Flash, T., Grasso, F. W., Hanlon, R. T., Hochner, B., Kier, W. M., Pagano, C. C., Rahn, C. D., and Zhang, Q. M., 2005,

"Continuum Robot Arms Inspired by Cephalopods," Unmanned Ground Vehicle Technology VII (Vol. 5804, pp. 303–314), SPIE.
[29] Fitzgerald, S. G., Delaney, G. W., and Howard, D., 2020, "A Review of Jamming Actuation in Soft Robotics," Actuators, **9**(4), p. 104.
[30] Jiang, A., Ranzani, T., Gerboni, G., Lekstutyte, L., Althoefer, K., Dasgupta, P., and Nanayakkara, T., 2014, "Robotic Granular Jamming: Does the Membrane Matter?," Soft Rob., **1**(3), pp. 192–201.
[31] Li, Y., Chen, Y., and Li, Y., 2018, "Distributed Design of Passive Particle Jamming Based Soft Grippers," 2018 IEEE International Conference on Soft Robotics (RoboSoft), Livorno, Italy, Apr. 24–28, pp. 547–552.
[32] Amend, J. R., Brown, E., Rodenberg, N., Jaeger, H. M., and Lipson, H., 2012, "A Positive Pressure Universal Gripper Based on the Jamming of Granular Material," IEEE Trans. Rob., **28**(2), pp. 341–350.
[33] Jiang, A., Xynogalas, G., Dasgupta, P., Althoefer, K., and Nanayakkara, T., 2012, "Design of a Variable Stiffness Flexible Manipulator With Composite Granular Jamming and Membrane Coupling," 2012 IEEE/RSJ International Conference on Intelligent Robots and Systems, Vilamoura-Algarve, Portugal, Oct. 7–12, pp. 2922–2927.
[34] Amend, J., Cheng, N., Fakhouri, S., and Culley, B., 2016, "Soft Robotics Commercialization: Jamming Grippers From Research to Product," Soft Rob., **3**(4), pp. 213–222.
[35] Jiang, P., Yang, Y., Chen, M. Z., and Chen, Y., 2019, "A Variable Stiffness Gripper Based on Differential Drive Particle Jamming," Bioinsp. Biomim., **14**(3), p. 036009.
[36] Wang, G., Li, M., and Zhou, J., 2019, "Modeling Soft Machines Driven by Buckling Actuators," Int. J. Mech. Sci., **157**, pp. 662–667.
[37] Coevoet, E., Escande, A., and Duriez, C., 2019, "Soft Robots Locomotion and Manipulation Control Using FEM Simulation and Quadratic Programming," 2019 2nd IEEE International Conference on Soft Robotics (RoboSoft), Seoul, South Korea, Apr. 14–18, pp. 739–745.
[38] Dilibal, S., Sahin, H., Danquah, J. O., Emon, M. O. F., and Choi, J.-W., 2021, "Additively Manufactured Custom Soft Gripper With Embedded Soft Force Sensors for an Industrial Robot," Int. J. Precis. Eng. Manuf., **22**(4), pp. 709–718.
[39] Beléndez, T., Neipp, C., and Beléndez, A., 2002, "Large and Small Deflections of a Cantilever Beam," Eur. J. Phys., **23**(3), pp. 371–379.
[40] Chen, L., 2010, "An Integral Approach for Large Deflection Cantilever Beams," Int. J. Non-Linear Mech., **45**(3), pp. 301–305.
[41] Khandan, R., Noroozi, S., Sewell, P., and Vinney, J., 2012, "The Development of Laminated Composite Plate Theories: A Review," J. Mater. Sci., **47**(16), pp. 5901–5910.
[42] White, P., Latscha, S., and Yim, M., 2010, "Modeling of a Dielectric Elastomer Bender Actuator," Actuators, **3**(3), pp. 245–269.
[43] Dratt, M., and Katterfeld, A., 2017, "Coupling of FEM and DEM Simulations to Consider Dynamic Deformations Under Particle Load," Gran. Matter, **19**(3), pp. 1–15.
[44] Cundall, P. A., and Strack, O. D., 1979, "A Discrete Numerical Model for Granular Assemblies," Geotechnique, **29**(1), pp. 47–65.
[45] Williams, J. R., Perkins, E., and Cook, B., 2004, "A Contact Algorithm for Partitioning N Arbitrary Sized Objects," Eng. Comput., **21**(2/3/4), pp. 235–248.
[46] Zang, M., Gao, W., and Lei, Z., 2011, "A Contact Algorithm for 3D Discrete and Finite Element Contact Problems Based on Penalty Function Method," Comput. Mech., **48**(5), pp. 541–550.
[47] Navarro, H. A., and de Souza Braun, M. P., 2013, "Determination of the Normal Spring Stiffness Coefficient in the Linear Spring–Dashpot Contact Model of Discrete Element Method," Powder Technol., **246**, pp. 707–722.
[48] Han, K., Peric, D., Owen, D., and Yu, J., 2000, "A Combined Finite/Discrete Element Simulation of Shot Peening Processes–Part II: 3D Interaction Laws," Eng. Comput., **17**(6), pp. 680–702.
[49] Marechal, L., Balland, P., Lindenroth, L., Petrou, F., Kontovounisios, C., and Bello, F., 2021, "Toward a Common Framework and Database of Materials for Soft Robotics," Soft Rob., **8**(3), pp. 284–297.